

MTL TR 86-7

*Army Materials and Mechanics Research Center
Technical Army Branch
Watertown, Massachusetts 02172*

AD A 167725

TENSILE AND FATIGUE BEHAVIOR OF ALUMINA FIBER REINFORCED MAGNESIUM COMPOSITES

JOHN NUNES and ERNEST S. C. CHIN

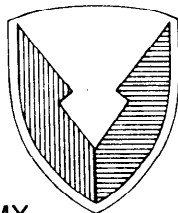
METALS RESEARCH DIVISION

JOHN M. SLEPETZ and NIKOLAOS TSANGARAKIS

MATERIALS INTEGRITY AND TESTING TECHNOLOGY DIVISION

March 1986

Approved for public release; distribution unlimited.



US ARMY
LABORATORY COMMAND
MATERIALS TECHNOLOGY
LABORATORY

U.S. ARMY MATERIALS TECHNOLOGY LABORATORY
Watertown, Massachusetts 02172-0001

The findings in this report are not to be construed as an official Department of the Army position, unless so designated by other authorized documents.

Mention of any trade names or manufacturers in this report shall not be construed as advertising nor as an official indorsement or approval of such products or companies by the United States Government.

DISPOSITION INSTRUCTIONS

Destroy this report when it is no longer needed.
Do not return it to the originator.

UNCLASSIFIED

SECURITY CLASSIFICATION OF THIS PAGE (When Data Entered)

REPORT DOCUMENTATION PAGE		READ INSTRUCTIONS BEFORE COMPLETING FORM
1. REPORT NUMBER MTL TR 86-7	2. GOVT ACCESSION NO.	3. RECIPIENT'S CATALOG NUMBER
4. TITLE (and Subtitle) TENSILE AND FATIGUE BEHAVIOR OF ALUMINA FIBER REINFORCED MAGNESIUM COMPOSITES		5. TYPE OF REPORT & PERIOD COVERED
		6. PERFORMING ORG. REPORT NUMBER
7. AUTHOR(s) John Nunes, Ernest S. C. Chin, John M. Slepetz, and Nikolaos Tsangarakis		8. CONTRACT OR GRANT NUMBER(s)
9. PERFORMING ORGANIZATION NAME AND ADDRESS U.S. Army Materials Technology Laboratory ATTN: SLCMT-MCM Watertown, MA 02172-0001		10. PROGRAM ELEMENT, PROJECT, TASK AREA & WORK UNIT NUMBERS D/A Project: 1L162105AH84 Agency Acces: DA OG7165
11. CONTROLLING OFFICE NAME AND ADDRESS U.S. Army Laboratory Command 2800 Powder Mill Road, Adelphi, MD 20783-1197		12. REPORT DATE March 1986
		13. NUMBER OF PAGES 24
14. MONITORING AGENCY NAME & ADDRESS (if different from Controlling Office)		15. SECURITY CLASS. (of this report) Unclassified
		15a. DECLASSIFICATION/DOWNGRADING SCHEDULE
16. DISTRIBUTION STATEMENT (of this Report) Approved for public release; distribution unlimited.		
17. DISTRIBUTION STATEMENT (of the abstract entered in Block 20, if different from Report)		
18. SUPPLEMENTARY NOTES Published in the Proceedings of the Fifth International Conference on Composite Materials sponsored by the TMS Composite Committee in San Diego, California, July 29, 30, August 1, 1985, p. 723-745.		
19. KEY WORDS (Continue on reverse side if necessary and identify by block number)		
Composite materials	Alumina fiber	Tension
Metal matrix composites	Mechanical properties	Residual stress
Magnesium	Fatigue	Fracture (mechanics)
20. ABSTRACT (Continue on reverse side if necessary and identify by block number) SEE REVERSE SIDE		

TENSILE AND FATIGUE BEHAVIOR OF ALUMINA FIBER REINFORCED
MAGNESIUM COMPOSITES

J. Nunes, E. S. C. Chin, J. M. Slepetz and N. Tsangarakis

Army Materials & Mechanics Research Center
Watertown, MA 02172
USA

Summary

Tensile and fatigue properties of as-cast polycrystalline alumina fiber reinforced magnesium (ZE41A) composites were determined as a function of fiber orientation and fiber content. Fiber dominant properties were studied on four fiber volume fractions of 35, 40, 45 and 55 percent at 24°C and 200°C testing temperatures. Off-axis, matrix dominant properties were investigated at a constant fiber volume fraction (55 percent) at 24°C. An attempt was also made to identify the effects of the fiber/matrix interface, matrix chemistry and residual stresses on the resultant mechanical behavior of these composites.

Introduction

Utilizing conventional casting fabrication techniques, lightweight structural alloys of aluminum and magnesium reinforced with polycrystalline alumina filaments (DuPont Fiber FP) have been available since the mid 1970's(1). These metal matrix composites offer the potential of a low cost, high performance material suitable for many weight savings applications(2). However, as with any new materials, their utilization depends on the existence of adequate mechanical property data base. In particular, the structure-property relationships within and between the constituents need to be characterized for this type of composite. Although some recent investigations on FP/Al(3,4) and FP/Mg(5,6) have addressed this problem, there still exists a need for a comprehensive study to identify the primary factors controlling the mechanical properties and failure characteristics of these composite materials.

In the present study, the tensile and fatigue behavior of as-cast FP/ZE41A (a magnesium casting alloy containing zinc, zirconium and rare earths) were determined as a function of fiber content and fiber orientation. The failure mechanisms for both fiber dominant and matrix dominant behavior were also investigated and compared to various failure theories which have been proposed earlier for metal matrix composites. The fiber dominant (0 degree fiber orientation) properties were studied on four volume fractions of 35, 40, 45 and 55 percent at 24°C and 200°C testing temperatures. Off-axis, matrix dominant properties were investigated on four angle-ply fiber orientations of 0, +22 1/2, +45 and 90 degrees at a constant fiber volume fraction (55 percent) at 24°C. An attempt was also made to identify the effects of the fiber/matrix interface, matrix chemistry and residual stresses on the resultant composite mechanical behavior.

Experimental Materials and Procedures

Materials

Polycrystalline alumina fiber (DuPont Fiber FP) reinforced magnesium cast plates with various fiber contents and fiber orientations were manufactured by E. I. DuPont de Nemours by liquid infiltration. Plates, 15.24 cm x 15.24 cm x 1.27 cm with the FP fibers uniaxially oriented and parallel to the plate length were fabricated with 35, 40, 45, and 55 percent fiber volume fractions. Angle-ply plates also were fabricated at a constant fiber volume fraction of 55 percent with +22 1/2 and +45 degree fiber orientations. Both longitudinal and transverse test coupons, 1.27 cm x 0.254 cm x 15.24 cm, were subsequently cut from the as-cast plates with the off-axis fibers oriented through the coupon thickness and parallel to the 15.24 cm x 0.254 cm surface.

A magnesium casting alloy, ZE41A, was chosen as the matrix material because of its excellent fiber/matrix interfacial strength and mechanical properties compared to unalloyed magnesium(6). Typical chemical analysis for the starting ingot material and the as-cast composite matrix alloy are given in Table I.

Table I.
 Typical ZE41A Ingot and Matrix Chemistry

Material	Zn	Zr	Rare Earths
	(w/o)		
AMS 4439 Spec	3.5 to 5.0	0.4 to 1.0	0.75 to 1.75
Ingot Material	4.4	0.3	0.9
Matrix	3.8	0.1	0.4

The as-cast matrix chemistry was determined by plasma emission spectrometry on solutions obtained by dissolving 0.2 gram samples in HCl without heating.

The composites were cast without adding reducible zirconium and rare earth halides to the remelted ingot which is normally required in order to maintain the desired zirconium and rare earth levels(7). Because of this the alloy depletion shown in Table I for the matrix was to be expected.

Metallographic examination of the test coupons (Figure 1) revealed a coarse matrix grain size between 0.1 to 0.2 mm. Occasionally much larger grains were also observed which extended throught the coupon thickness, of 2.5 mm.

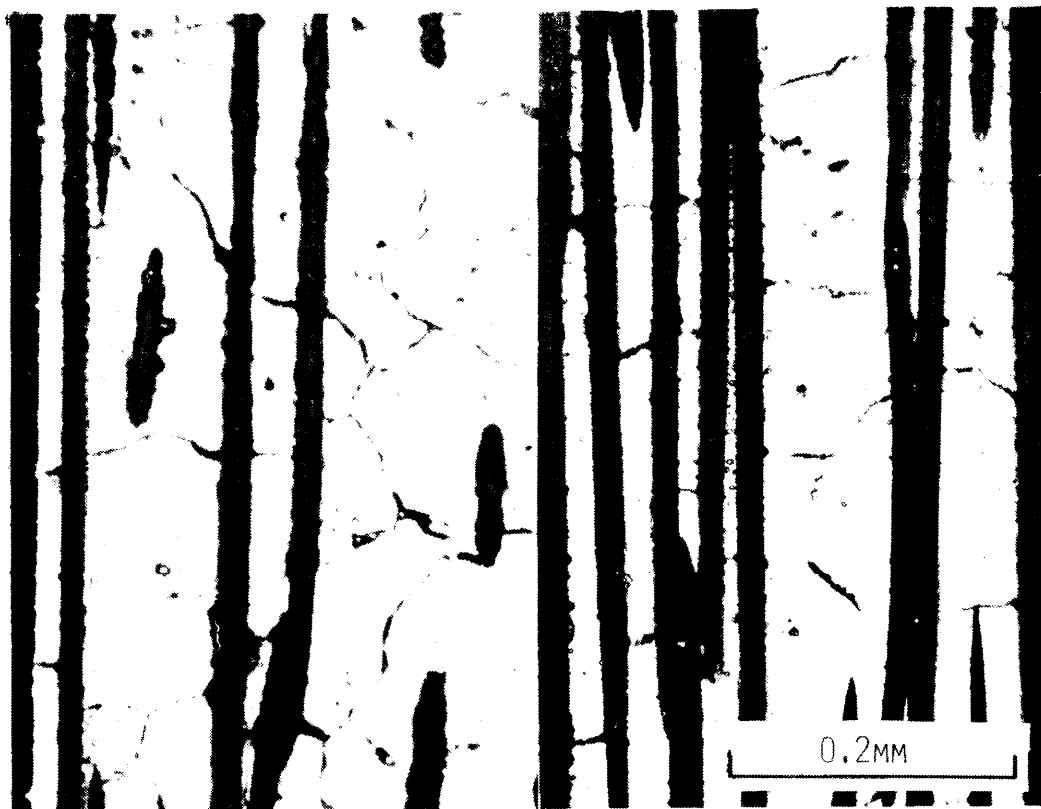


Figure 1. Grain size of as-cast FP/ZE41A magnesium matrix material.

Filament diameters (d_f), fiber volume fractions (V_f) and composite densities (ρ) were measured on representative test coupons for each of the as-cast plates received (Table II).

Table II.
Fiber Volume Fractions, Fiber Diameters and Densities of As-Cast
FP/ZE41A Plates

Plate No.	N	V_f (%)	d_f^* (μm)	ρ (g/cm^3)
300 CE-65	8	35.3 \pm 2.8	19.6 \pm 0.4	2.53 \pm 0.05
200 CE-2	10	39.9 \pm 3.6	19.8 \pm 0.5	2.57 \pm 0.05
200 CE-6	4	45.0 \pm 1.8	19.5 \pm 0.3	2.71 \pm 0.02
181 KD-2	4	54.0 \pm 2.9	19.2 \pm 0.2	2.95 \pm 0.02
164 KD-6	7	54.9 \pm 1.3	19.7 \pm 0.3	2.99 \pm 0.01
164 KD-7	6	56.0 \pm 1.8	19.8 \pm 0.2	2.97 \pm 0.02
200 CE-7	4	56.0 \pm 2.2	19.3 \pm 0.1	2.95 \pm 0.04

N = Number of test coupons examined.

* Diameter measurements were metallographically made on 100 filaments on each of the coupons examined.

A least squares fit of the V_f and ρ values including a matrix density measurement of 1.82 g/cm^3 gave the following rule of mixtures relationship with a correlation coefficient of 0.995.

$$\rho = 2.08 V_f \times 10^{-2} + 1.80 \text{ g/cm}^3$$

The mechanical and physical characteristics of DuPont's fiber FP and the composite consolidation process employed are described elsewhere(1-3).

Mechanical Test Procedures

In an earlier study(4), it was found that rectangular specimens with bonded tabs, commonly employed in fatigue studies of metal matrix composites, were inadequate especially at elevated test temperatures because failure usually occurred in the tab. Satisfactory fatigue test results were obtained using an untabbed streamline contoured specimen previously developed for testing organic matrix composites (8) shown in Figure 2. The streamline contour is designed to minimize the transverse tensile and shear stresses in the transition region and to produce a uniform maximum axial stress in the minimum width section. Streamline specimens were machined from the FP/ZE41A coupons as described in reference (8) and were used to determine both tensile and fatigue properties. As with FP/Al specimens, machining damage to the edges of FP/Mg specimens was observed from photomicrographs and found to consist of a zone of broken filaments extending to a depth of 0.05 mm beneath the surface.

Tensile tests were conducted at room temperature (RT) in a 90 KN capacity screw driven test machine and at 200°C in a closed loop servo-hydraulic test machine (44.5 KN capacity) at a cross-head speed of $8.5 \times 10^{-4} \text{ cm/sec}$. Biaxial strain gages were mounted on both sides of the specimens for measuring longitudinal and transverse strain. Tension tests were run on virgin and fatigue runout specimens. Before loading to failure, each virgin specimen was subjected to several loading cycles between zero and approximately 80% of the ultimate tensile strength. This

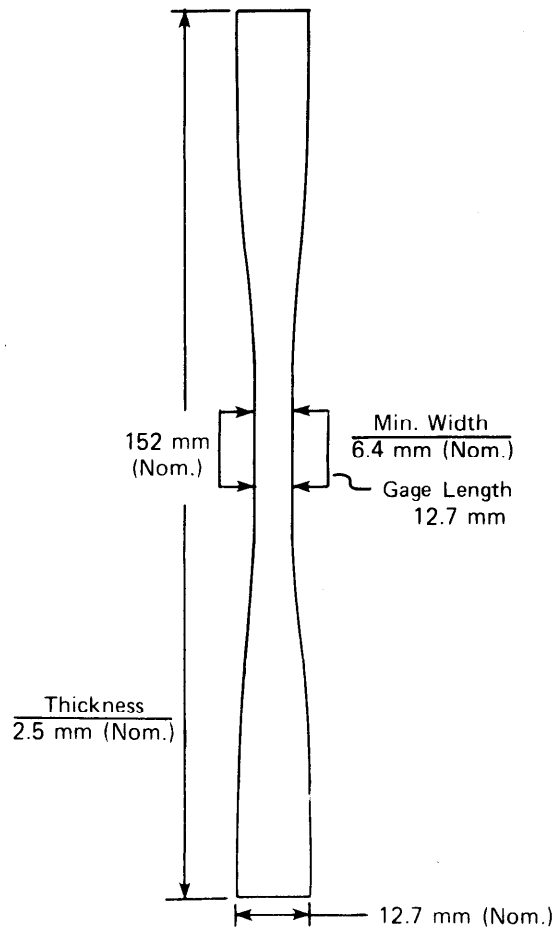


Figure 2. Tensile and fatigue test specimen configuration.

procedure enabled any cyclic changes in the hysteresis loop to be recorded and provided additional information about the fatigue damage mechanisms. Fatigue runout specimens were cycled several times, duplicating the fatigue loading range, before loading to failure. This was done to observe any change in the elastic modulus resulting from the fatigue loading. Initial tangent modulus (E), ultimate tensile strength (UTS), strain to fracture (ϵ_{fr}) and Poisson's ratio (ν) were determined from the load vs strain records.

All fatigue tests were conducted at RT and 200°C in the 44.5 kN closed loop servo-hydraulic fatigue test machine at 40 Hz under load control at an R-ratio of 0.1 (the minimum cyclic stress divided by the maximum cyclic stress.) Serrated grips were employed in all tests. Some fatigue specimens were strain-gaged to provide a dynamic load-strain response (during cyclic loading) on an oscilloscope. When it was desired to obtain a static load-strain curve, testing was interrupted periodically and a static test was executed under manual control. In this way, the tangent modulus under both static and dynamic conditions, was continuously monitored.

Elevated temperatures tests were conducted in a clam shell furnace containing quartz heating elements. The temperature was held to $\pm 2^\circ\text{C}$ and monitored continuously with 4 thermocouples attached directly to each specimen.

Transmission Electron Microscopy

Thin foils of FP/ZE41A were prepared for transmission electron microscopy (TEM) through various steps of mechanical thinning and ion milling. The composite specimens were then viewed and examined with the JEOL 200CX TEMSCAN at 200KV. The thinned foils were tilted to a two beam diffracting condition for imaging. Selective area diffractions were performed to identify unknown phases in the matrix and at the interface.

Results and Discussion

Microstructural Analysis

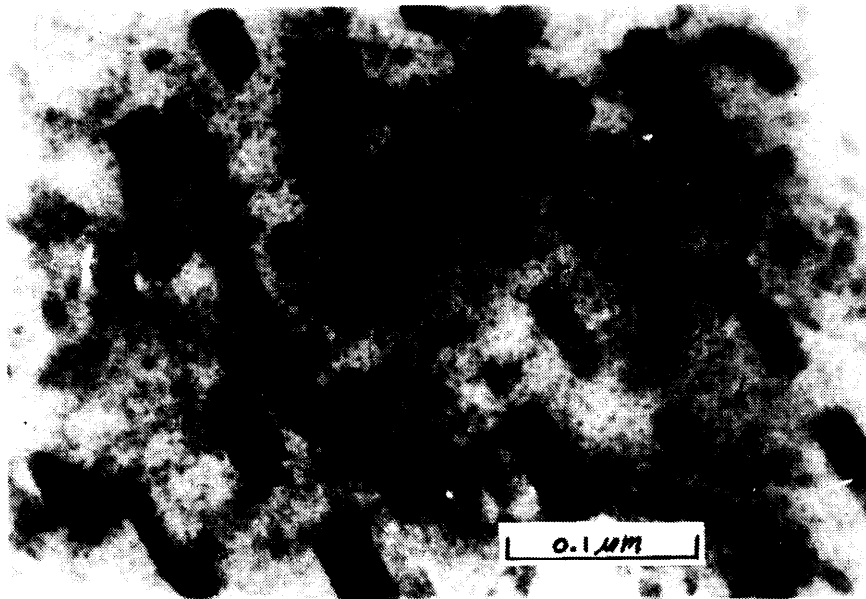
Transmission electron microscopic examination of the thinned composite foils revealed uniformly distributed dislocations and precipitates (Figure 3) throughout the matrix. The average dislocation density measured was 10^{10} cm^{-2} (Figure 3a) which is representative of a cold worked metal and not an annealed or as-cast metal. The latter would normally have a dislocation density of 10^6 to 10^8 cm^{-2} . Apparently, the development of residual stresses during cooling from the solidification temperature caused intensive plastic deformation in the ZE41A Mg alloy. Work hardening would also accompany this highly localized plastic flow as room temperature is approached. Both of these factors would lead to the relatively high dislocation density found in the as-cast matrix. The rod and spherical shaped precipitates shown in Figure 3b were identified by microdiffraction as MgZn' and MgZn respectively. It was found that the MgZn' precipitate was much more prevalent than the MgZn. Other, less predominant types of precipitate were also observed but were not identified.

Metallographic analysis also revealed an elongated second phase that appeared to originate at the fiber. In many instances this phase was found to be bridged with one or more filaments. Energy dispersive analysis (EDA) revealed that this is a zinc rich phase which also contains some evidence of the rare earth, cerium. No sign of zirconium could be found nor was zirconium coring(9) evident in any of the phases examined. The zirconium obviously remains in solid solution in these composites. Although most of the composite plates appeared to exhibit a matrix alloy content representative of the bulk ingot material (Table 1), one exception was encountered. Plate 300CE-65, 35.3% V_f , exhibited twice the zinc and five times the zirconium levels normally found in the other composite plates. Because the actual processing history of these composites is largely unknown and considered proprietary by the producer, the exact cause of the increase in alloy content could not be explained.

Examination by TEM of the fiber/matrix interface (Figure 4) revealed a 0.25 micron wide reaction zone consisting of submicron MgO particles and fine precipitates of the spinel, $\text{MgO} \cdot \text{Al}_2\text{O}_3$. Microdiffraction identification of the $\text{MgO} \cdot \text{Al}_2\text{O}_3$ spinel confirmed an earlier bulk analysis reported on this composite(10). Correspondingly, the MgO identification also confirmed a recently published result(6). A more detailed discussion of the analytical procedures and results employed in this study is given elsewhere(11).

Adjacent to the reaction zone and surrounding each fiber there was a one micron thick layer of matrix material. Within this layer, submicron, equiaxed grains of magnesium were also found distributed along the fiber interface. Both precipitates and dislocations were not as evident in this layer as that found outside of it in the remainder of the matrix.

Apparently during the early stages of solidification, a skin forms on each fiber which is surrounded by semi-molten metal. When solidification is completed, several fibers will have been entrapped within a single grain (see Figure 1). The development of an in situ coating provides a beneficial means for mitigating potentially harmful residual stresses at the fiber/matrix interface. Differential thermal contraction strains between the ceramic fiber (coefficient of thermal expansion (CTE) at 20°C = $6.8 \times 10^{-6} \text{ }^\circ\text{C}^{-1}$) and the metal matrix (CTE at 20°C = $26 \times 10^{-6} \text{ }^\circ\text{C}^{-1}$) can be quite large. The in situ coated fiber is analogous to the ceramic-metal transition zones developed to obtain well bonded ceramic to metal seals.



(a)



(b)

Figure 3. Transmission electron microscopy of FP/ZE41A magnesium matrix showing (a) precipitates and (b) dislocations.



(a)



(b)

Figure 4. Transmission electron microscopy of FP/ZE41A fiber/matrix interfacial area.
(RZ = reaction zone, Mg = magnesium alloy and Al_2O_3 = FP fiber.)

Volume Fraction Effects

Figure 5 illustrates typical tensile load-strain curves obtained on the uniaxially oriented FP/ZE41A virgin and fatigue runout specimens. In Figures 6 and 7, the fatigue S-N curves are shown for the various volume fractions tested along with the unreinforced matrix material. The mechanical properties derived from the tensile and the fatigue test results are summarized in Table III.

The load-strain behavior of the virgin specimen in Figure 5 shows that during the unload-reload sequence, a hysteresis loop develops due to the occurrence of cyclic plastic deformation in the matrix. In an earlier study(13) it was shown that both tensile and compressive yielding of the matrix must occur to obtain this type of hysteresis in a metal matrix composite. Intermittent tensile tests performed during fatigue testing in this study revealed that these hysteresis loops gradually decrease in area with increasing cycles and completely close after 10^2 to 10^3 cycles. During the first few loading cycles some changes in the tangent modulus were also observed. Both the closing of the hysteresis loop and the initial change in tangent modulus are probably due to matrix work hardening effects. (Without work hardening, the hysteresis loop and the tangent modulus would remain essentially constant(13) and tensile and compressive yielding would continue to occur throughout the entire cyclic life of the specimen.) Once the hysteresis loop closed, the intermittent tensile load-strain curves remained essentially linear and constant, independent of any additional number of cycles applied. The unload-reload tensile curve shown in Figure 5 for the runout specimen was typical of fatigue specimens monitored in this study.

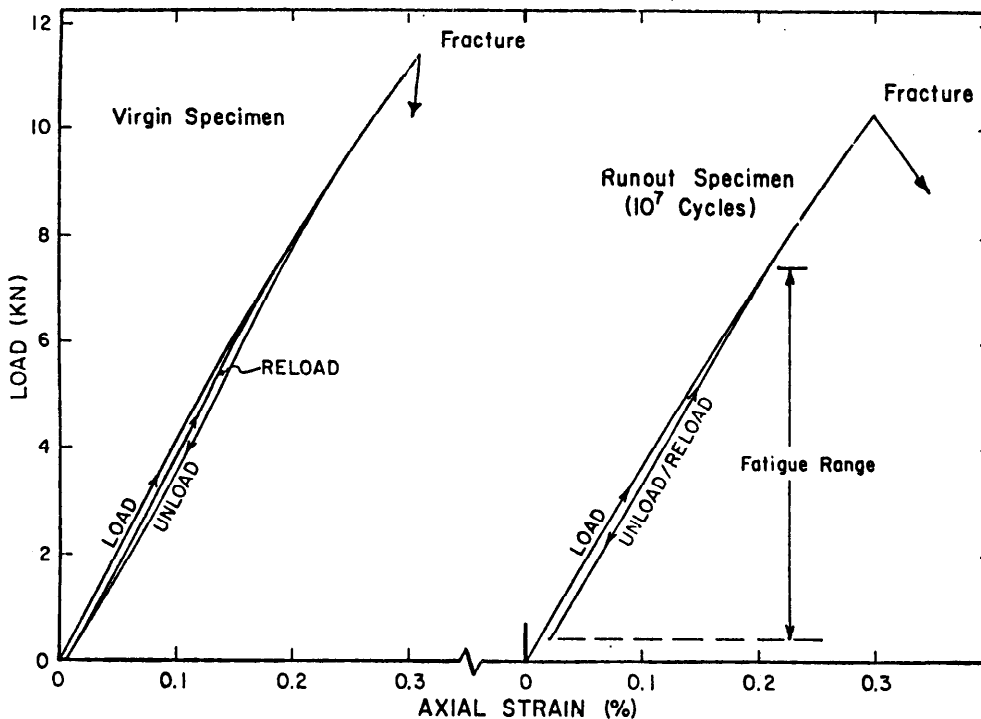


Figure 5. Static tensile deformation curves for virgin and fatigue runout composite test specimens.

The fatigue curves obtained for FP/SE41A at 24°C, shown in Figures 6 and 7 resemble the sigmoidal S-N shape found in most metals and not the shape usually found in fiber reinforced materials where the fatigue strength gradually (and usually linearly) decreases with increasing cyclic life. At 24°C the fatigue strength apparently levels off at 10^4 to 10^6 cycles depending on the fiber content. (It should be noted that the 35 percent V_f composite does not follow these nor other observed trends due to a difference in matrix alloy content which will be discussed further on.) The 200°C fatigue curves are more representative of most metal matrix composites including FP/Al(4) and FP reinforced unalloyed magnesium(5). No abrupt decrease in fatigue strength is apparent prior to reaching the 10^7 cycle endurance limit. Except for the 35 percent V_f composite, the 24°C and the 200°C S-N curves all intersect at two points. These are the 10^4 cycle endurance limit and depending on the fiber content a higher fatigue stress between 10^4 to 10^6 cycles.

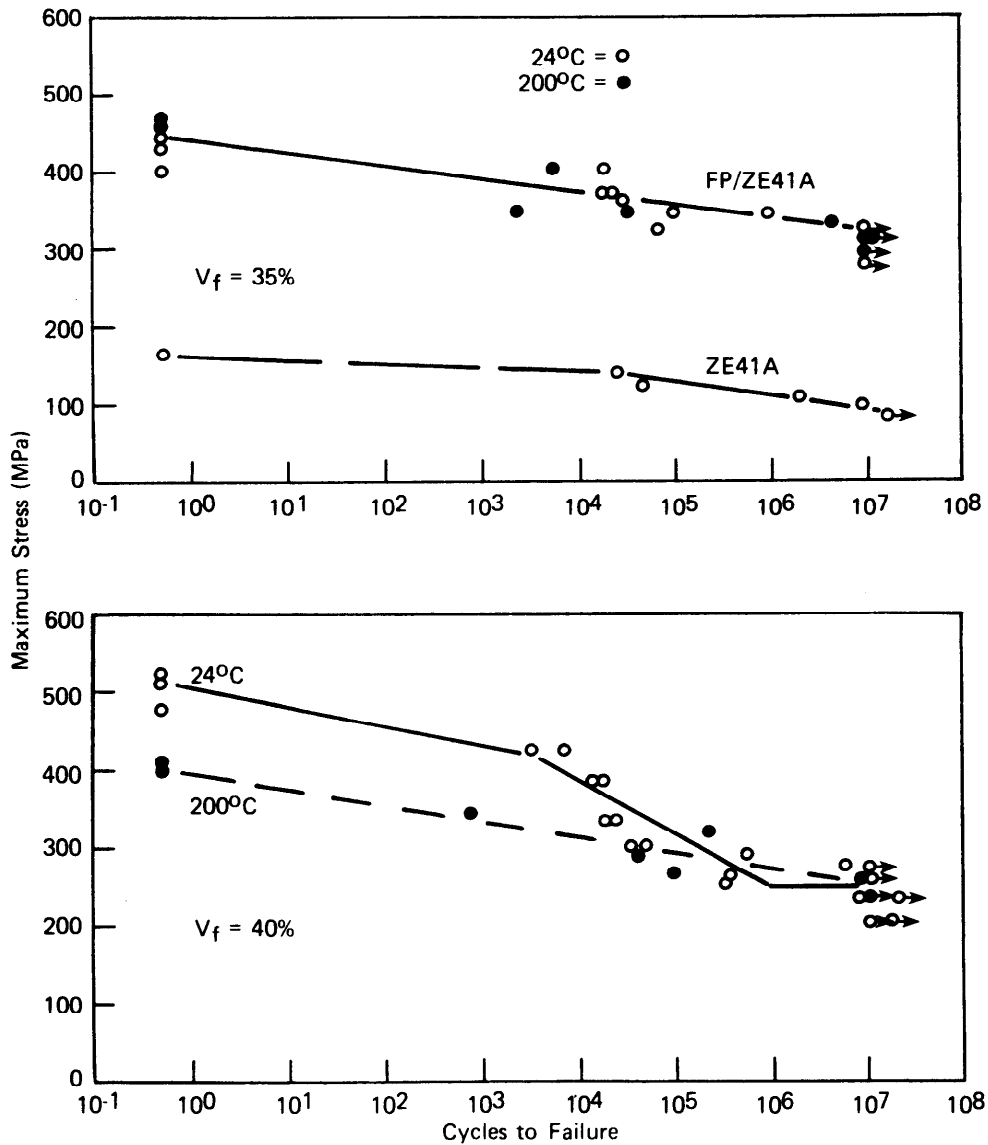


Figure 6. Fatigue curves for uniaxially fiber-oriented FP/ZE41A at 24°C and 200°C for 35 and 40 percent fiber volume fractions, (R = 0.1).

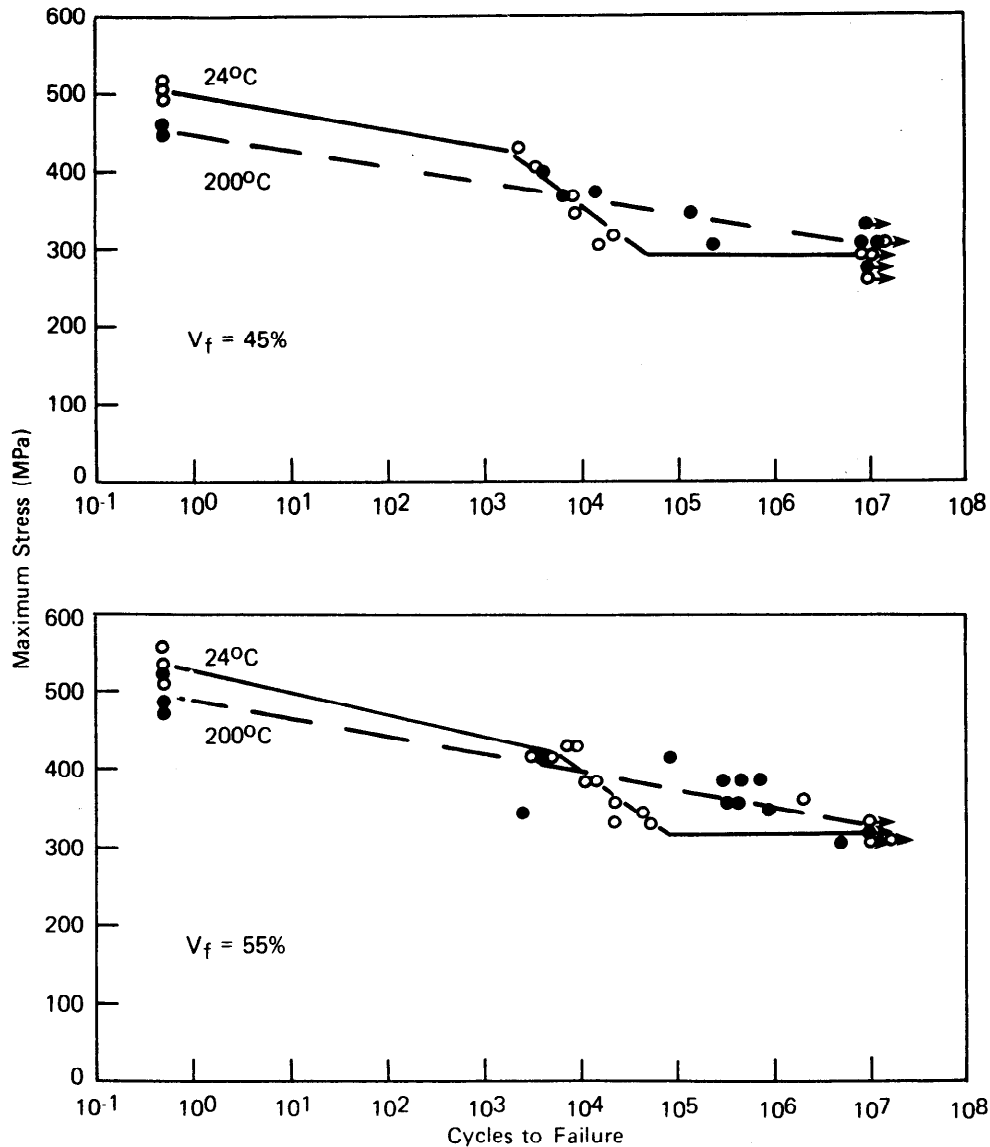


Figure 7. Fatigue curves for uniaxially fiber-oriented FP/ZE41A at 24°C and 200°C for 45 and 55 percent fiber volume fractions, ($R = 0.1$).

It has been proposed(14) that two types of fatigue S-N curve can be obtained for fiber reinforced composites depending upon different fatigue damage mechanisms which involve either transverse or longitudinal crack growth. When the fiber/matrix interface is very strong and the fiber/matrix strength ratio is relatively low, transverse crack growth is assumed to occur leading to a sigmoidal S-N curve such as that found in this study at 24°C and usually found in most metals. On the other hand, when the fiber/matrix interface is weak and the fiber/matrix strength ratio relatively high, longitudinal crack growth along the fiber/matrix interface is assumed to occur and under ideal conditions failure occurs at the bundle strength of the filaments resulting in a horizontal S-N curve. However, in most composites where filament debonding predominates, failure occurs at fatigue stress levels well below the bundle strength due to the development of an interconnected network of weak fiber fracture sites throughout the composite cross-section. In the latter case, the shape of the S-N curve falls between the two extremes just described similar to the curves found in this study at 200°C. It should also be noted that extensive debonding

is not a necessary condition for obtaining non-sigmoidal fatigue curves as they have been found in FP/Al(4) where the dominant failure mode was the linking up of accumulated fiber fractures without evidence of longitudinal crack growth. The essential factor apparently controlling the shape of the S-N curve is the degree of departure from planar, Mode I type crack growth (sigmoidal shape) toward a mixed mode crack growth or bundle failure (non-sigmoidal/linear shape).

Tensile test results on the 10^7 runout specimens revealed a decrease in both the ultimate tensile strength ($\Delta\sigma_{UTS}$) and the tangent modulus (ΔE) with increasing fiber content (Figure 8) when compared to results obtained on virgin test specimens. At fiber volume fractions above 40-45 percent, $\Delta\sigma_{UT}$ and ΔE actually indicate higher properties than the virgin material and are only lower beyond this range of volume fractions. As mentioned previously the changes in modulus observed on the fatigue runout specimens all occurred within the first few loading cycles and were more likely due to work hardening effects and not due to fatigue damage such as debonding and crack growth. On the other hand, the residual tensile strength results obtained on the runout specimens are an indication that some fatigue damage such as accumulative random fiber fracture(4) did occur.

Table III.

Tensile and Fatigue Properties of FP/ZE41A Mg and Ze41A Mg (As-Cast)

Test Temperature = 240C										
V _f (%)	‡ (deg's)	E (GPa)	E*	σ_{UTS}	σ_{UTS}^*	σ_{EL}	ν	ϵ_{fr} (%)	N	N*
0	-	45	-	163	-	90	0.35	6.0	4	-
35.3	0	145	152	442	466	324	0.26	0.35	8	6
39.9	0	164	148	510	427	248	0.26	0.35	4	5
45.0	0	168	171	503	499	290	0.25	0.32	4	4
54.9	0	216	208	532	445	317	0.23	0.25	4	4
56.0	0	210	-	532	-	-	0.25	0.28	4	-
52.6	±22-1/2	163	161	410	400	186	0.22	0.34	4	3
53.6	±45	136	119	296	296	152	0.23	0.56	4	2
54.0	90	108	105	228	228	131	0.30	0.36	7	4
Test Temperature = 200C										
0	-	41	-	118	-	-	0.28	16.0	3	-
35.3	0	150	154	459	450	317	0.26	0.32	3	3
39.9	0	139	141	406	390	248	0.25	0.32	2	1
45.0	0	171	171	452	414	303	0.24	0.28	2	3
53.0	0	208	205	494	465	331	0.24	0.25	4	4

Nomenclature:

V_f = Fiber volume fraction.

‡ = Fiber orientation.

E, E* = Tangent modulus of virgin and 10^7 cycle runout specimens respectively.

σ_{UTS} , σ_{UTS}^* = Ultimate tensile strength of virgin and 10^7 cycle runout specimens respectively.

N, N* = Number of virgin and 10^7 cycle runout specimens tested respectively.

ν = Poisson's ratio.

ϵ_{fr} = Tensile strain to fracture.

σ_{EL} = Endurance limit at 10^7 cycles (maximum runout stress obtained on a minimum of 2 specimens).

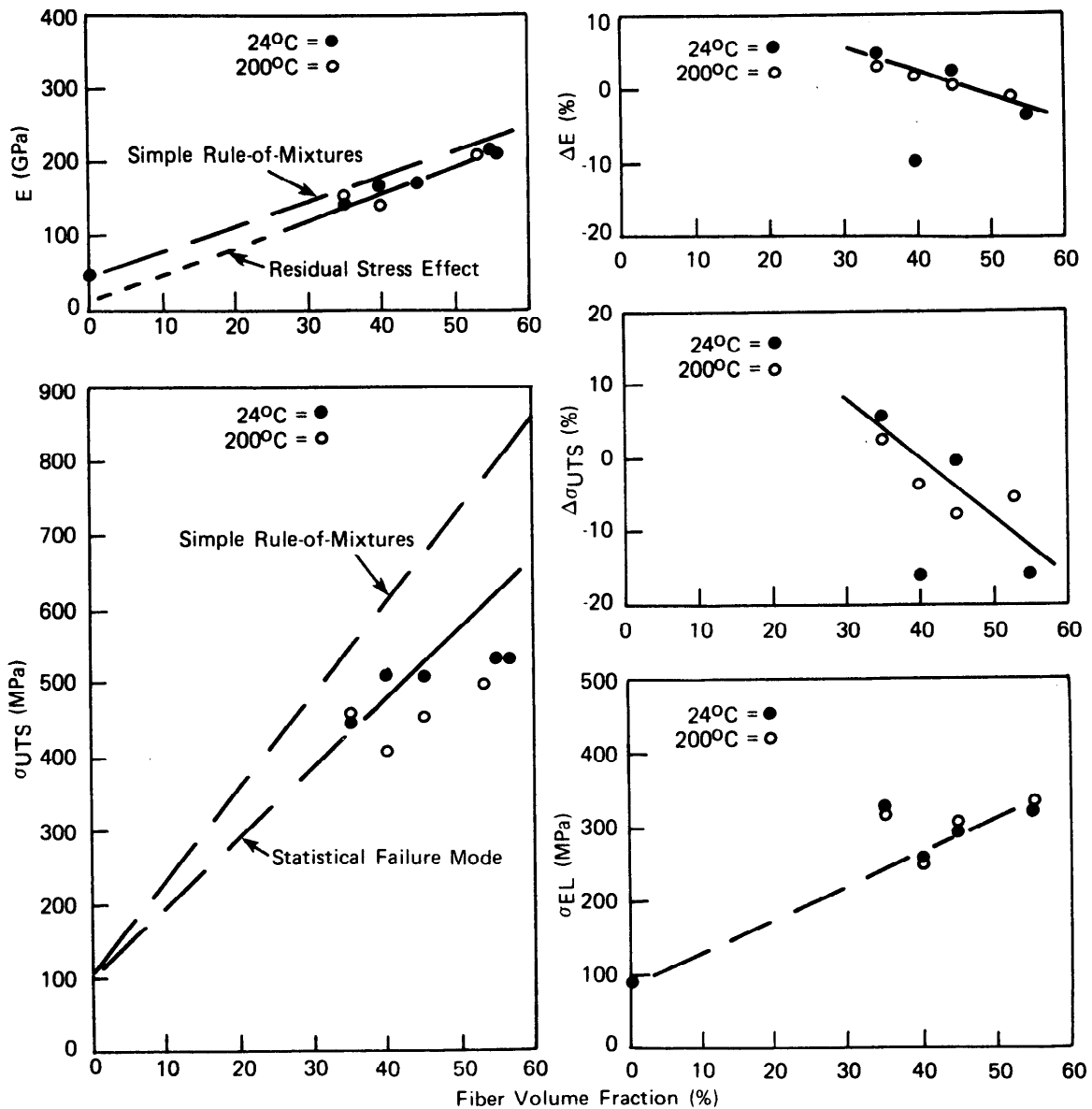


Figure 8. Effect of fiber volume fraction on the mechanical properties of uniaxially fiber-oriented FP/ZE41A. (σ_{UTS} = ultimate tensile strength, σ_{EL} = endurance limit, and E = tangent modulus. $\Delta\sigma_{UTS}$ and ΔE = changes in the virgin composite σ_{UTS} and E observed on fatigue runout specimens.)

As expected the mechanical properties of these composites were significantly affected by fiber content. Also, except for the shape of the S-N curves, there were no significant differences between the 24°C and the 200°C test results. Both of these findings reflect the dominant role played by the uniaxially oriented FP fiber whose properties remain unchanged at these temperatures. This is shown in Figure 8 where the tangent modulus, the ultimate tensile strength and the endurance limit are all seen to increase with increasing fiber content yet are unaffected by the test temperature change. An exception to this trend can be seen in the 35.3 percent V_f composites. Anomalous increases in the 200°C tensile strength and the 24°C and the 200°C endurance limits were obtained apparently due to a difference in the matrix alloy content. As mentioned earlier, the matrix had five times the zirconium and twice the zinc levels normally encountered in this composite. A previous study(12) has indicated

that the increases in zinc and particularly in zirconium contents encountered here can result in a 33 to 200 percent increase in the yield and ultimate tensile strengths of the ZE41A alloy. Such increases in matrix properties would readily translate into improved composite properties(6) provided no adverse interactions occur at the fiber/matrix interface.

The apparent linear correlation between fiber content and the tangent modulus, ultimate tensile strength and endurance limit shown in Figure 8 suggests that a rule-of-mixtures relationship might exist for these composite properties. However, to demonstrate a rule-of-mixtures relationship it was first necessary to determine the in situ constituent properties and the initial stress state for the composite. A reasonably good rule-of-mixtures correlation was obtained for both the tangent modulus and the ultimate tensile strength when residual stresses in the matrix and filament tensile strength variations were taken into account.

Because plastic deformation and work hardening of the matrix apparently occur as soon as a tensile load is applied to the composite due to the presence of a residual tensile stress, a simple rule-of-mixtures prediction for the composite tangent modulus that is solely based on elastic behavior cannot apply. This is shown in Figure 8 where a simple rule-of-mixtures curve based upon a fiber modulus (E_f) of 379 GPa and a matrix modulus (E_m) of 45 GPa did not show agreement with the experimental composite modulus data. On the other hand, a very good correlation was obtained (Figure 8) when elastic-plastic behavior of the composite is accounted for as in the following modified rule-of-mixtures equation;

$$E_c = V_f E_f + V_m \frac{d\sigma}{d\epsilon} \quad (1)$$

A value of 10 GPa was assumed for $\Delta\sigma/\Delta\epsilon$ to obtain the modified curve in Figure 8. In equation (1), the matrix is assumed to have been work hardened to a residual stress level that is proportional to the differential thermal contraction strains experienced during cooling from the composite casting temperature to room temperature. Figure 9 illustrates the experimental tensile stress-strain curve at 24°C and the corresponding change in slope $d\sigma/d\epsilon$ of the unreinforced ZE41A magnesium alloy. Also shown is the idealized stress-strain curve obtained after differential thermal contraction prestrain. The appropriate $\Delta\sigma/\Delta\epsilon$ value was assumed to remain unchanged over a strain range (ϵ_c) equivalent to that used in obtaining the composite tangent modulus (approximately 0.1 percent strain). An estimate of the matrix prestrain was obtained by assuming that the matrix stress-strain relations were independent of temperature over the range of interest. For tensile prestrains of up to 6×10^{-3} , the experimental matrix stress-strain curve was approximated by the following simple power law relationship:

$$\sigma_m = S_1 \epsilon_m^n \quad (2)$$

where:

$$\begin{aligned} S_1 &= 1367 \text{ MPa} \\ n &= 0.5 \end{aligned}$$

With the above assumptions, a simplistic, one dimensional model was used to compute the residual stresses in the matrix as follows:

$$0 = \Delta T(\alpha_f - \alpha_m) + \epsilon_m + \epsilon_f \quad (3)$$

where:

$\Delta T = 175^\circ\text{C}$ (Assumed temperature increment where significant residual stresses are retained in the matrix.)

α_f, α_m = Coefficients of fiber ($6.5 \times 10^{-6}/^\circ\text{C}$) and matrix ($26 \times 10^{-6}/^\circ\text{C}$) thermal expansion respectively.

ϵ_f, ϵ_m = Fiber and matrix prestrains respectively.

Using the assumed power law relationship for the matrix stress-strain behavior and a linear elastic stress-strain relationship for the fiber, Equation 3 can be rewritten as:

$$0 = \Delta T(\alpha_f - \alpha_m) + \frac{\sigma_f}{E_f} + \left(\frac{\sigma_m}{S_1}\right)^{1/n} \quad (4)$$

Also because of static equilibrium, the fiber load must equal the matrix load and therefore Equation 4 can be further reduced to the following equation;

$$0 = \Delta T(\alpha_f - \alpha_m) - \frac{V_m \sigma_m}{V_f E_f} + \left(\frac{\sigma_m}{S_1}\right)^{1/n} \quad (5)$$

Solving Equation 5 for the case of $V_f = V_m = 0.5$ and $E = 379 \text{ GPa}$ results in $\sigma_m = 81 \text{ MPa}$ and $\epsilon_m = 3.5 \times 10^{-3}$. For other volume fractions of interest (0.2 to 0.8), σ_m does not vary significantly.

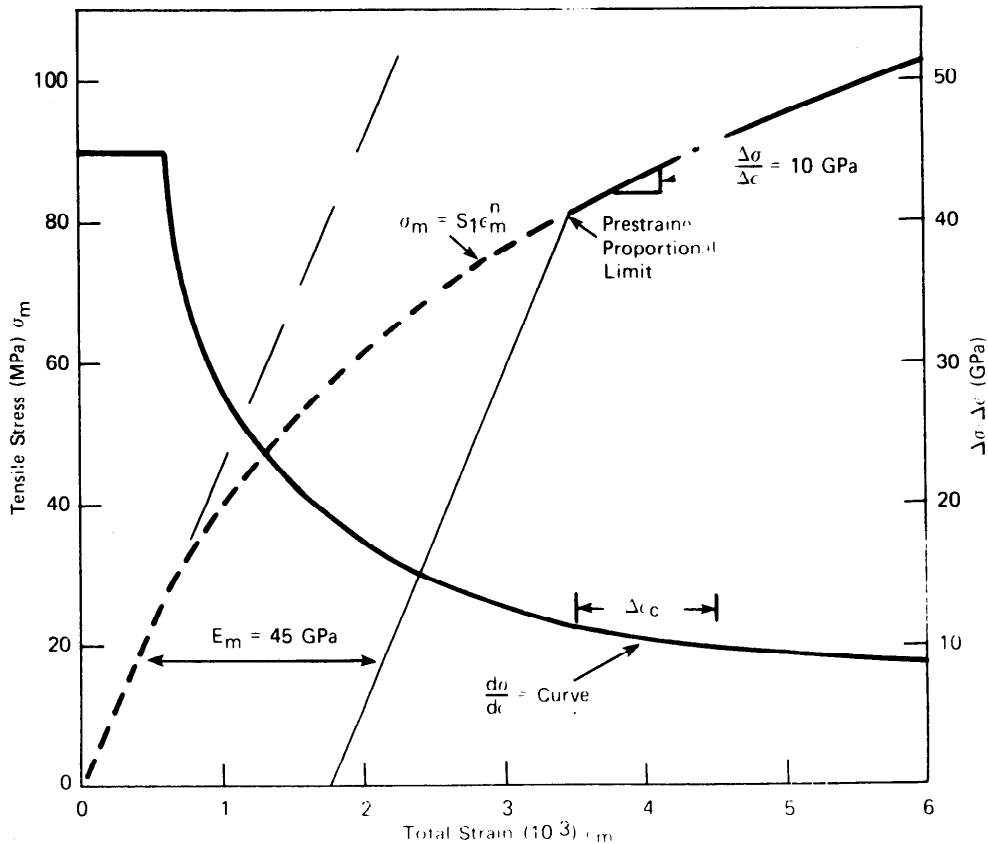


Figure 9. Tensile stress-strain behavior of ZE41A magnesium before and after prestraining.

In order to reconcile the experimental composite tensile strength values to a rule-of-mixtures law, it is necessary to take into account the in situ statistical distribution of filament strength and its dependence on fiber length. Previously, good agreement between experimental results and rule-of-mixtures strength predictions was obtained for FP/Al(3) and SiC/Al(15) when a two-parameter Weibull distribution function was used in conjunction with a lower bound statistical failure stress analysis proposed by Zweben(16). A similar approach was employed for the FP/ZE41A in this study, also with good results as seen in Figure 8. The statistical lower bound fiber failure stress $\bar{\sigma}_2$ and the composite σ_{UTS} are obtained from the following equations:

$$\bar{\sigma}_2 = \sigma_0 \left[4N\ell\delta(k^m-1) \right]^{-1/2m} \quad (6)$$

$$N\ell = v_f v_c / a_f \quad (7)$$

$$\delta = d_f \left[\frac{1}{2} (E_f / G_m) (v_f^{-1/2} - 1) \right]^{1/2} \quad (8)$$

where: $\sigma_0 = 1840 \text{ MPa} \cdot \text{cm}^{1/m}$, Weibull normalizing constant
 $M = 6.5$, Weibull flaw sensitivity constant
 $N = \text{number of fibers}$
 $\ell = \text{fiber gage length}$
 $\delta = \text{ineffective gage length}$
 $k = 1.146$, stress concentration factor for square array
 $v_c = 2.46 \text{ cm}^3$, composite volume
 $d_f = 20.3 \text{ } \mu\text{m}$, filament diameter
 $G_m = 16.5 \text{ GPa}$, matrix shear modulus
 $E_f = 379 \text{ GPa}$, fiber tensile modulus

Substituting equations 7 and 8 into equation 6 results in the following;

$$\bar{\sigma}_2 = s_0 \left[v_f (v_f^{-1/2} - 1) \right]^{-1/2m} \quad (9)$$

where for the values given above,

$$s_0 = 958 \text{ MPa}$$

Equation 9 is valid over the fiber volume fractions of interest, e.g., at v_f of 0.3, $\bar{\sigma}_2 = 1066 \text{ MPa}$ and at $v_f = 0.6$, $\bar{\sigma}_2 = 1096 \text{ MPa}$. Using equation 9, a modified rule-of-mixtures relationship also can be written as;

$$\sigma_{UTS} = v_f \left[s_0 (v_f^{3/2} - v_f^2)^{-1/4m} - \sigma_m \right] + \sigma_m \quad (10)$$

Examination of both tensile and fatigue specimens after failure revealed a planar fracture surface topography containing plateau areas that were 100 to 200 mm in depth. None of the specimens showed signs of a single fracture origin site nor was there any evidence of debonding or fiber pull-out. Apparently the final fracture event consisted of joining the plateau areas which contained a relatively high concentration of random

fiber breaks that accumulated either from the increasing static load or from the constant cyclic load. Specimens tested at 200°C exhibited more matrix ductility than specimens tested at room temperature. There appeared to be more necking down and pulling away of the matrix at the fiber fracture sites. In only one instance was there evidence of matrix cracking. This was observed on a 200°C fatigue specimen that failed after 8×10^6 cycles. Several other fatigue specimens showed signs of secondary cracking across fibers terminating in the matrix and multiple fiber breaks in the vicinity of the fractured surface.

Orientation Effects

The tensile stress-strain behavior of virgin and runout, off-axis specimens is similar to that seen in the uniaxially oriented composites (Figure 5) except that the hysteresis loop (area enclosed by the unload-reload curve) increases in area with increasing fiber orientation angle. Also, as with the uniaxial orientation, the hysteresis loop closes after 10^5 to 10^6 cycles due to matrix work hardening. The area of the hysteresis loop represents an energy loss per cycle which was found to increase from about 1 percent at the zero degree fiber orientation to 16 percent at the 90 degree fiber orientation. It should be noted that the unreinforced, as-cast ZE41A exhibited an even greater hysteresis loss. Values of approximately 40 percent were observed under initial tension loading for the unreinforced matrix.

The effect of fiber orientation on the fatigue S-N curve is shown in Figure 10. Similar to the room temperature uniaxial case, the +45 degree off-axis composites exhibited a sigmoidal shaped curve that leveled off between 10^5 to 10^6 cycles. On the other hand, the 90 degree fiber oriented composite exhibited a more linear S-N curve with no apparent leveling off. For comparison, the unreinforced matrix S-N curve is also shown in Figure 10.

Off-axis fiber reinforced composites would be expected to exhibit a more matrix dominant type of behavior with their mechanical properties approaching the matrix properties as the fiber orientation angle increased. This is shown in Figure 11 for the tangent modulus, the ultimate tensile strength and the endurance limit. In each case the off-axis properties exceeded the matrix properties for all orientations. The relatively high values of off-axis mechanical properties observed are evidence of a strong fiber/matrix interfacial bond. If the bond were poor, as in the case of graphite/epoxy, these properties would be degraded to values even lower than the unreinforced matrix. In fact, in the case of the 90° orientation, the tensile strength and endurance limit were over 40 percent higher than for the unreinforced ZE41A matrix; and the modulus was 140 percent higher.

The tensile test results obtained on the 10^7 cycle runout specimens revealed little change in the tangent modulus (ΔE) compared to the virgin material. The only exception to this was for the +45 degree fiber orientation where an abrupt modulus decrease of 12 percent occurred (Figure 11). As mentioned earlier these changes in the modulus all occurred within the first few loading cycles and were apparently due to matrix work hardening effects. In all cases, the monitored tangent modulus values obtained beyond these first few cycles remained essentially constant indicating little or no fatigue damage due to debonding or crack growth. It is worth noting that the total strain to failure ϵ_{fr} reached a maximum at the +45° orientation. In contrast, the residual tensile strength ($\Delta \sigma_{UTS}$) of the runout specimens was found to decrease below and remain unchanged above +45 degrees indicating that fatigue damage such as accumulative fiber fracture had only occurred below this orientation.

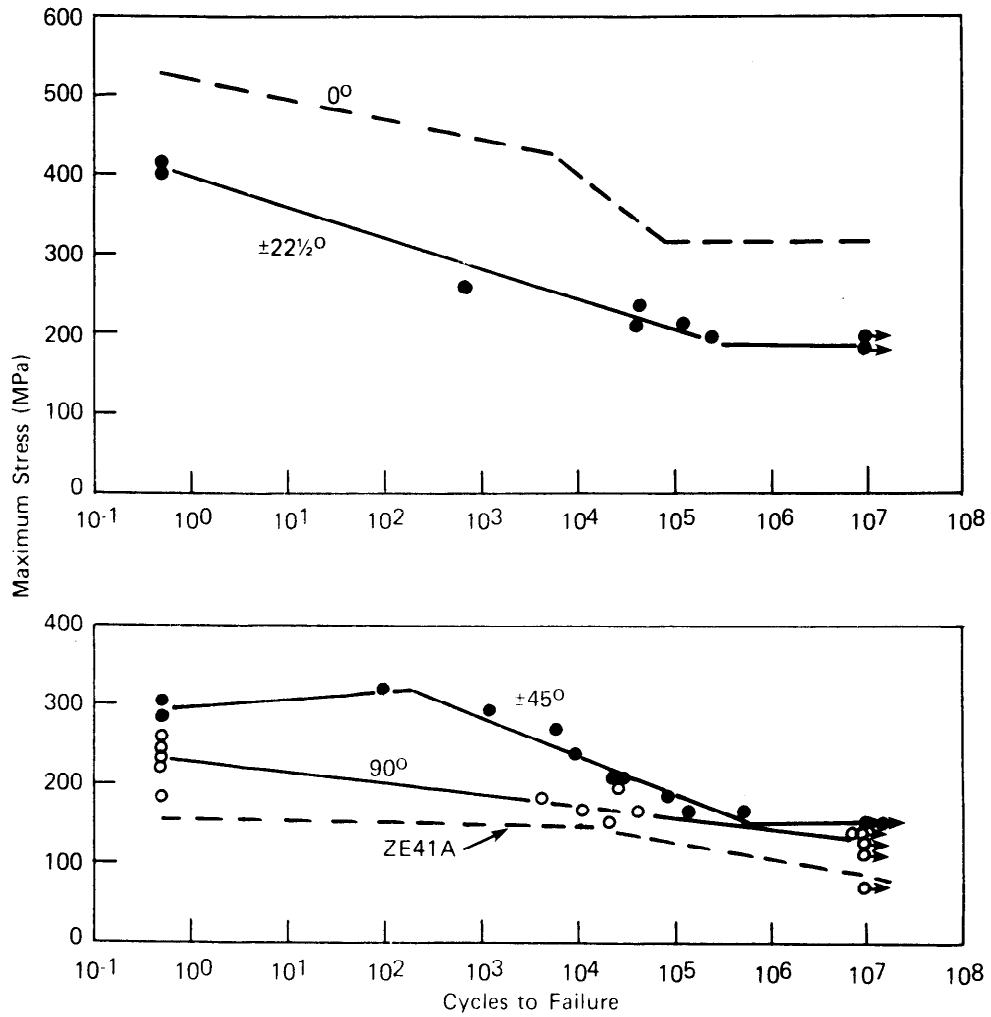


Figure 10. Fatigue curves for off-axis fiber-oriented FP/ZE41A at 24°C for constant fiber volume fraction of 55 percent, (R = 0.1).

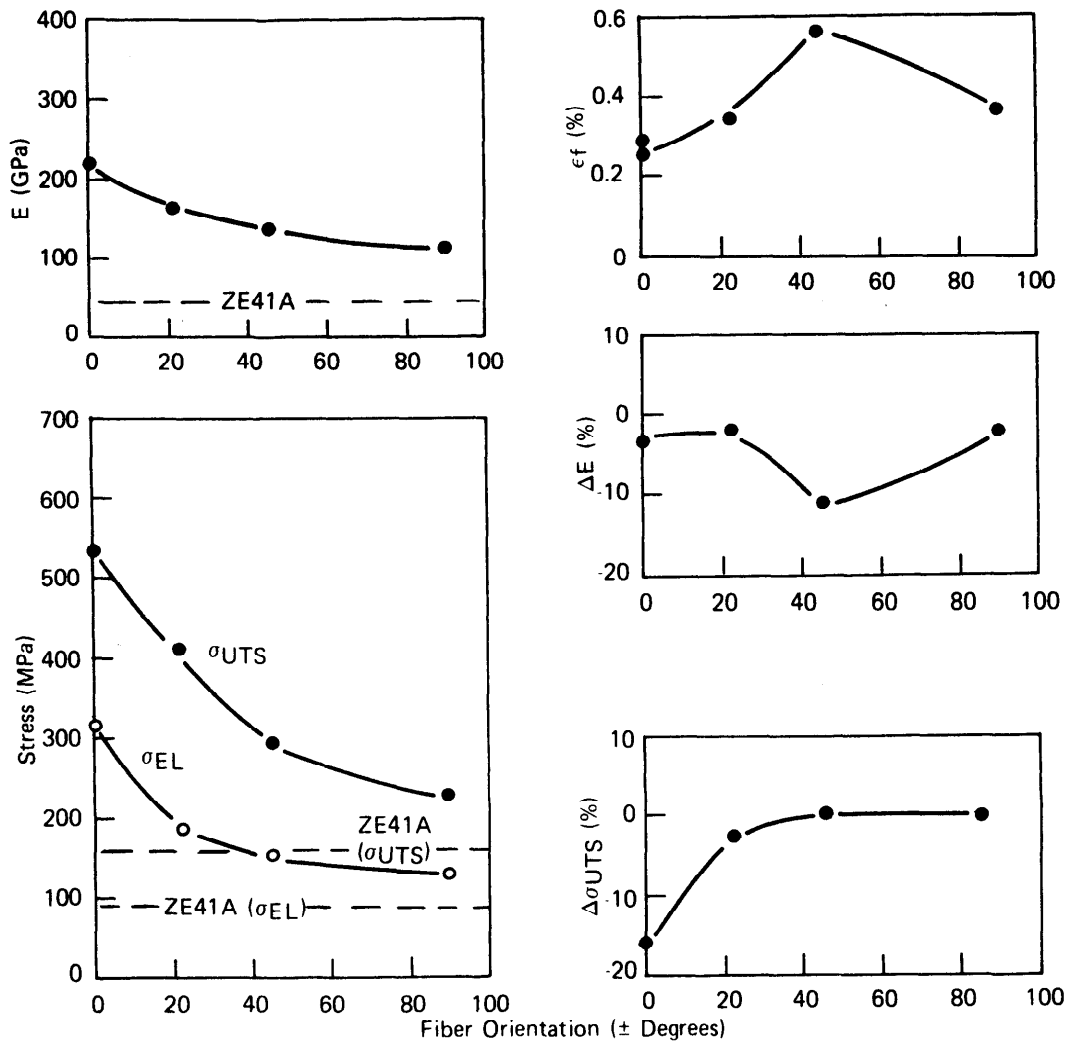
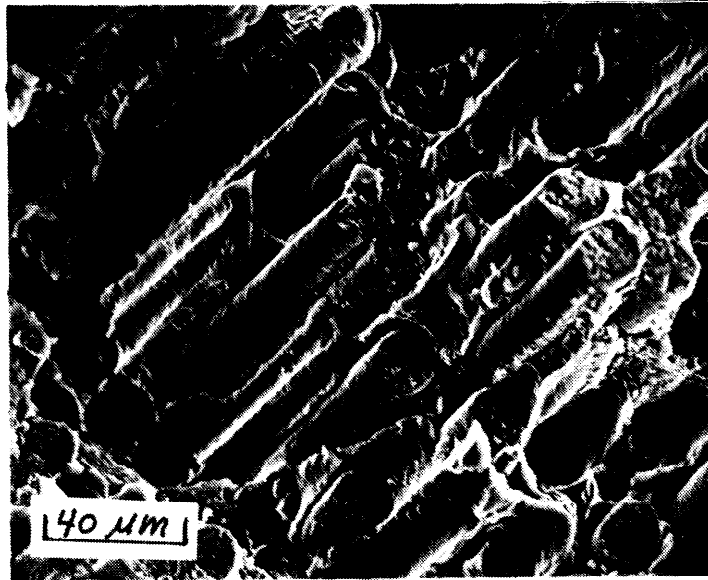
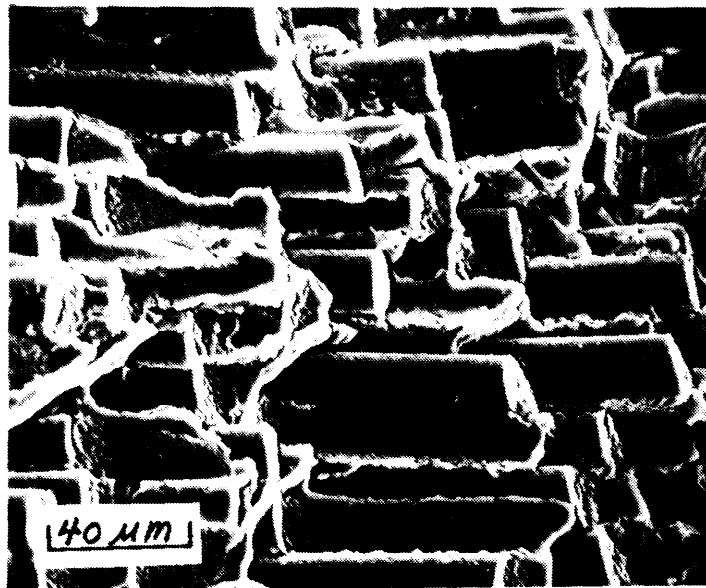


Figure 11. Effect of fiber orientation on the mechanical properties of FP/ZE41A at constant fiber volume fraction of 55 percent. (σ_{UTS} = ultimate tensile strength, σ_{EL} = endurance limit, E = tangent modulus, and ϵ_{fr} = tensile fracture strain. $\Delta\sigma_{UTS}$ and ΔE = changes in the virgin composite σ_{UTS} and E observed on fatigue runout specimens.)

No significant differences in fracture surface topography were evident between the tensile and the fatigue specimens. The fracture surfaces of the ± 45 degree specimens had an irregular topography that corresponded to the off-axis laminations. On the other hand the $\pm 22\ 1/2$ degree composite fracture surfaces were relatively flat. In both cases, the fibers appeared to have failed under localized tensile loads normal to the fiber axis with no signs of debonding or matrix shear (Figure 12a). On the other hand the 90 degree composite fractured surfaces revealed failures along the fiber interface, fiber splitting and localized fiber bending fractures (Figure 12b).



(a)



(b)

Figure 12. Scanning electron micrographs of typical fatigue fracture surfaces on off-axis fiber-oriented FP/ZE41A. (a) ± 45 degrees and (b) 90 degrees. (Static tensile failures exhibited essentially the same fracture surface topography.)

Conclusions

1. The fiber/matrix interface contains a reaction zone on the order of 0.25 microns in width consisting of submicron MgO particles and very fine MgO.Al₂O₃ precipitates. Adjacent to the reaction zone and surrounding each fiber there is approximately a one micron thick layer of alloy metal that initially forms during solidification. Subsequent fusion of these in situ matrix coated fibers is therefore accomplished with a more gradual transition of the fiber and matrix differential thermal contraction strains.
2. Progressive random fiber fracture was found to be the dominant damage mechanism controlling the fatigue and static tensile strengths of FP/ZE41A. The final fracture event occurred when a sufficient number of broken filaments accumulated at a particular composite cross-section. Except for the ± 45 degree and the 90 degree fiber orientations, this failure mode appeared under all test conditions studied.
3. The tangent modulus was not significantly affected by fatigue loading up to 10⁷ cycles. Small changes in the tangent modulus sometimes occurred during the early cyclic stages (10² to 10³ cycles). On the other hand, the residual tensile strength of 10⁷ cycle fatigue runout specimens was found to decrease with increasing fiber content and decreasing fiber orientation due to accumulative fiber damage effects.
4. Analytical predictions of the composite tangent modulus for the unidirectional fiber orientation could only be accomplished by considering elastic-plastic behavior of the matrix. This was necessitated by the initial stress state of the composite which contained residual stresses in the matrix equal to its proportional limit. A simple analytical model was employed to obtain an approximation of the residual stress and the corresponding work hardening slope of the matrix.
5. Using a two parameter Weibull distribution function and a lower bound statistical failure mode analysis to estimate the in situ filament tensile strengths, a good correlation was obtained between the theoretical and experimental tensile strengths in unidirectional composites.
6. The off-axis mechanical properties decreased with increasing fiber orientation angle to minimum values that always exceeded the bulk matrix properties. For example, the tangent modulus was 40 percent higher and the ultimate tensile strength and the fatigue endurance limit was 40 percent higher than the unreinforced matrix for the 55 percent V_f FP/ZE41A composite.
7. The matrix alloy chemistry showed a strong effect on the composite's mechanical properties. A composite whose matrix had double the zinc and five times the zirconium contents normally found in this alloy exhibited significantly improved tensile and fatigue properties.

References

1. Champion, A.R., Krueger, W.H., Hartman, H.S. and Dhingra, A.K., "Fiber FP Reinforced Metal Matrix Composites" in Proceedings of the International Conference of Composite Materials, Metallurgical Society of AIME, April 1978, pp 883-904.
2. Krueger, W.H. and Dhingra, A.K., "Alumina Fiber Reinforced Metal Composites for Potential Automotive Engine Applications" Presented at the American Institute of Chemical Engineers" Detroit, MI, August 1981.
3. Nunes, J., "Tensile Property Evaluation of Polycrystalline Alumina Filaments and Their Composites," Composites Technology Review, Vol. 5, No. 2, 1983, pp 53-60.
4. Tsangarakis, N., Slepetz, J.M. and Nunes, J., "Fatigue Behavior of Alumina-Fiber Reinforced Aluminum Composites" in Proceedings 2nd US/Japan Conference on Composite Materials, 1984.
5. Hack, J.E., Page, R.E. and Levereant, G.R., "Tensile and Fatigue Behavior of Aluminum Oxide Fiber Reinforced Magnesium Composites: Part I. Fiber Fraction and Orientation," Metallurgical Transactions A, Vol. 15A, 1984, pp 1389-1396.
6. Page, R.E., Hack, J.E., Sherman, R. and Leverant, G.R., "Tensile and Fatigue Behavior of Aluminum Oxide Fiber Reinforced Magnesium Composites: Part II. Alloying Effects" Metallurgical Transactions A, Vol. 15A, 1984, pp 1397-1405.
7. Emley, E.F. and Fisher, P.A., "The Control of Quality of Magnesium - Base Alloy Castings," Journal of the Institute of Metals, Vol. 85, Part 6, 1956-57, pp 236-254.
8. Oplinger, D.W., Gandhi, K. and Parker, B., "Studies of Tension Test Specimens for composite Materials," Army Materials and Mechanics Research Center, AMMRC TR 82-27, April 1982.
9. Emley, E.F., "Principals of Magnesium Technology" Pergamon Press, New York, (1966) pp 256-259.
10. Chin, E.S.C., "An Investigation of the Interfacial Phenomena in FP (α -Al₂O₃) Fiber Reinforced Magnesium Composite" MS Thesis, Division of Engineering, Brown University, Providence RI (1983).
11. Chin, E.S.C., "Transmission Electron Microscopy of Alumina Fiber Reinforced Magnesium Composite" (to be published).
12. Lagowski, B. "Effect of Composition and Heat Treatment on the Tensile Properties of ZE41 (Mg-4Zn-1RE-0.17Zr) Casting Alloy" American Foundrymen's Society Transactions, Vol. 85 (1977) pp 237-240.
13. Nunes, J. "Vibration damping and Isolation with Energy Absorbing Composites" Shock and Vibration Bulletin, No. 44, The Shock and Vibration Information Center, Naval Research Labs, Wash. D.C. (1974) pp 23-42.
14. Gouda, M., Prewo, K.M. and McEvily, A.J., "Mechanism of Fatigue in Boron-Aluminum Composites" Fatigue of Fibrous Composite Materials, ASTM STP 723 (1981) pp 101-115.

15. Nunes, J. "Tensile Behavior of Silicon Carbide Filaments and Silicon Carbide Fiber Reinforced 6061 Aluminum" to be published NBS Proceedings 39th Mechanical Failure Prevention group Meeting, "Failure Mechanisms in High Performance Materials" (1984).
16. Zweben, C., Smith, W.S. and Wardle, M.W., "Test Methods for Fiber Tensile Strength, Composite Flexural Modulus and Properties of Fabric Reinforced Laminates" Fifth Conf. on Composite Materials Testing and Design, ASTM STP 674 (1979) pp 228-262.

No. of
Copies

To

Commander, U.S. Army Electronics Research and Development Command,
Fort Monmouth, NJ 07703
1 ATTN: AMDSD-L
1 AMDSD-E

Commander, U.S. Army Foreign Science and Technology Center, 220 7th Street,
N.E., Charlottesville, VA 22901
1 ATTN: Military Tech, Mr. Marley

Commander, U.S. Army Materiel Systems Analysis Activity,
Aberdeen Proving Ground, MD 21005
1 ATTN: AMXSY-MP, H. Cohen

Commander, U.S. Army Missile Command, Redstone Arsenal, AL 35898
1 ATTN: Technical Library
1 AMSMI-RLM
1 AMSMI-RLA, Dr. James J. Richardson

Commander, U.S. Army Belvoir Research and Development Center, Fort Belvoir,
VA 22060
1 ATTN: STRBE-D
1 STRBE-G
1 STRBE-X
1 STRBE-N
1 STRBE-VL

Commander, U.S. Army Research and Technology Labs, Applied Technology Laboratory
(AVSCOM), Fort Eustis, VA 23604
1 ATTN: AMDAR-ATL-ATP, Mr. James Gomez, Aerospace Engineer

Commander, U.S. Army Tank-Automotive Command, Warren, MI 48090
1 ATTN: AMSTA-RCKM

Director, Benet Weapons Laboratory, LCWSL, USA AMCOM, Watervliet, NY 12189
1 ATTN: AMSMC-LCB-TL
1 AMSMC-LCB-PS, Dr. I. Ahmad

David Taylor Naval Ship Research and Development Center, Annapolis, MD 21402
1 ATTN: Dr. Michael Vassilaros - Code 2814

Office of Naval Technology, 800 N. Quincy Street, Arlington, VA 20017
1 ATTN: Mr. J. J. Kelly - Code MAT 0715

Naval Research Laboratory, Washington, DC 20375
1 ATTN: Dr. C. I. Chang - Code 5830
1 Dr. G. R. Yoder - Code 6384
1 Dr. S. C. Sanday - Code 6370

Chief of Naval Research, Arlington, VA 22217
1 ATTN: Code 471
1 Dr. Steven G. Fishman

DISTRIBUTION LIST

No. of
Copies

To

- 1 Office of the Under Secretary of Defense for Research and Engineering,
The Pentagon, Washington, DC 20301
- 2 Commander, Defense Technical Information Center, Cameron Station, Building 5,
5010 Duke Street, Alexandria, VA 22314
- Metals and Ceramics Information Center, Battelle Columbus Laboratories,
505 Avenue, Columbus, OH 43201
- 1 ATTN: Mr. Robert J. Fiorentino, Program Manager
- 1 Defense Advanced Research Projects Agency, Defense Sciences Office/MSD,
1400 Boulevard, Arlington, VA 22209
- Headquarters, Department of the Army, Washington, DC 20314
- 1 ATTN: DAEN-RDM, Mr. J. J. Healy
- Commander, U.S. Air Force Wright Aeronautical Laboratories, Wright-Patterson
Air Force Base, OH 45433
- 1 ATTN: AFWAL/MLC
- 1 AFWAL/MLLP, D. M. Forney, Jr.
- 1 AFWAL/MLBC, Mr. Stanley Schulman
- 1 AFWAL/MLLS, Dr. Terence M. F. Ronald
- 1 AFWAL/FIBEC, Dr. Steve Johnson
- 1 Edward J. Morrissey, AFWAL/MLTE, Wright-Patterson Air Force Base, OH 45433
- Commander, Army Research Office, P.O. Box 12211, Research Triangle Park,
NC 27709
- 1 ATTN: Information Processing Office
- 1 Dr. George Mayer
- Commander, U.S. Army Materiel Command, 5001 Eisenhower Avenue, Alexandria,
VA 22333
- 1 ATTN: AMCLD
- Commander, U.S. Army Armament, Munitions and Chemical Command,
Dover, NJ 07801
- 1 ATTN: AMDAR-SCM, J. D. Corrie
- 1 Mr. Harry E. Peibly, Jr., PLASTECH, Director
- Commander, U.S. Army Aviation Systems Command, 4300 Goodfellow Blvd., St. Louis,
MO 63120
- 1 ATTN: AMDAV-NS, Harold Law
- Director, U.S. Army Ballistic Research Laboratory, Aberdeen Proving Ground,
MD 21005
- 1 ATTN: AMDAR-TSB-S (STINFO)

No. of
Copies

To

- 1 Mr. Louis A. Gonzalez, Kaman Tempo, 816 State Street, Santa Barbara, CA 93101
- 1 Prof. James G. Goree, Dept. of Mechanical Engineering, Clemson University,
Clemson, SC 29631
- 1 William F. Grant, AVCO Specialty Materials Division, 2 Industrial Avenue,
Lowell, MA 01851
- 1 Mr. Jacob Gubbay, Charles Stark Draper Laboratories, 555 Technology Square,
Mail Station 27, Cambridge, MA 02139
- 1 Mr. John E. Hack, Southwest Research Institute, 6220 Culebra Road,
San Antonio, TX 78284
- 1 Dr. H. A. Katzman, The Aerospace Corporation, P.O. Box 92957
Los Angeles, CA 90009
- Lockheed California Company, Burbank, CA 91520
- 1 ATTN: Mr. Rod F. Simenz, Department of Materials and Processes
- Lockheed Georgia Company, 86 South Cobb Drive, Marietta, GA 30063
- 1 ATTN: Materials and Processes Engineering Department
- 1 Mr. James Carroll
- 1 Mr. Patrick J. Moore, Staff Engineer, Lockheed Missiles and Space Company,
Organization 62-60, Building 104, P.O. Box 504, Sunnyvale, CA 94086
- 1 R. Byron Pipes, Professor & Director, Center for Composite Materials,
University of Delaware, Newark, DE 19711
- 1 Dr. Karl M. Prewo, Principal Scientist, United Technologies Research Center,
Mail Stop 24, East Hartford, CT 06108
- 1 Dr. B. W. Rosen, Materials Sciences Corporation, Gwynedd Plaza 11, Bethlehem
Pike, Spring House, PA 19477
- 1 Prof. Marc H. Richman, Division of Engineering, Brown University,
Providence, RI 02912
- 1 Mr. Ronald P. Tye, Energy Materials Testing Laboratory, Biddeford Industrial
Park, Biddeford, ME 04005
- 1 Mr. Robert C. Van Siclen, Vought Corporation, Advanced Technology Center,
P.O. Box 226144, Dallas, TX 75266
- 1 Prof. Franklin E. Wawner, Department of Materials Science, School of Engineering
and Applied Sciences, University of Virginia, Charlottesville, VA 22903
- 1 Dr. Carl Zweben, General Electric Company, Valley Forge Space Center/M4018,
P.O.Box 8555, Philadelphia, PA 19101

No. of
Copies

To

1 Naval Sea Systems Command, Washington, DC 20362
1 ATTN: Mr. Marlin Kinna - 62R4

1 Naval Air Development Center, Warminster, PA 18974
1 ATTN: Dr. E. U. Lee - Code 60632

1 Naval Surface Weapons Center, White Oak, Silver Spring, MD 20910
1 ATTN: John V. Foltz - Code R32
1 Dr. Herbert Newborn - Code R34

1 National Aeronautics and Space Administration, Washington, DC 20546
1 ATTN: Mr. G. C. Deutsch - Code RW
1 Mr. Michael A. Greenfield, Program Manager for Materials, Code RTM-6

1 National Aeronautics and Space Administration, Lewis Research Center,
Cleveland, OH 44135
1 ATTN: Dr. James A. DiCarlo, Mail Stop 106-1

1 National Aeronautics and Space Administration, Marshall Space Flight Center,
Huntsville, AL 35812
1 ATTN: R. J. Schwinghammer, EH01, Dir, M&P Lab
1 Mr. W. A. Wilson, EH41, Bldg. 4612

1 The Boeing Vertol Company, P.O. Box 16858, Philadelphia, PA 19142
1 ATTN: Mr. Robert L. Pinckney, Mail Stop P62-06
1 Mr. Joseph W. Lenski, Jr., Mail Stop P32-09

1 E. I. DuPont De Nemours and Company, Inc., Textile Fibers Department,
Pioneering Research Laboratory, Experimental Station, Wilmington, DE 19898
1 ATTN: Blake R. Bichlmeir
1 Joyce W. Widrig

1 Mr. Rex C. Claridge, TRW, Incorporated, Manufacturing Division,
Mail Stop 01-2210, 1 Space Park, Redondo Beach, CA 90278

1 Dr. James A. Cornie, Materials Processing Center, Bldg. 8, Room 237,
Massachusetts Institute of Technology, 77 Massachusetts Avenue,
Cambridge, MA 01239

1 Dr. Bhagwam K. Das, Engineering Technology Supervisor, The Boeing Company,
P.O. Box 3999, Seattle, WA 98124

1 Leroy Davis, NETCO, 2225 East 28th Street, Building 5, Long Beach, CA 90806

1 Mr. Joseph F. Dolowy, Jr., President, DWA Composite Specialties, Inc.,
21133 Superior Street, Chatsworth, CA 91311

1 Mr. Robert E. Fisher, President, AMERCOM, Inc., 8948 Fullbright Avenue,
Chatsworth, CA 91311

No. of
Copies

To

1 Dr. Carl Zweben, General Electric Company, Valley Forge Space Center/M4018,
P.O. Box 8555, Philadelphia, PA 19101

Commander, U.S. Army Laboratory Command, 2800 Powder Mill Road, Adelphi,
MD 20783-1197

1 ATTN: Technical Library

Director, U.S. Army Materials Technology Laboratory, Watertown, MA 02172-0001

1 ATTN: SLCMT-IML

4 Authors